Available online at www.sciencedirect.com
ScienceDirect
Trans. Nonferrous Met. Soc. China 35(2025) 3751−3760
Transactions of Nonferrous Metals Society of China
www.tnmsc.cn

Dispersion of nano-TiB in Ti64 based composite through plasma rotating electrode process followed by spark plasma sintering

Wen-qi LIU[1], Shuai WANG[1], Xin CHEN[1], Lu-jun HUANG[1,2], Jia-yi JIN[1], Feng-bo SUN[1], Wei-hang LU[1], Lin GENG[1,2]

1. School of Materials Science and Engineering, Harbin Institute of Technology, Harbin 150001, China;
2. State Key Laboratory of Precision Welding & Joining of Materials and Structures, Harbin Institute of Technology, Harbin 150001, China

Received 9 January 2024; accepted 4 September 2024

Abstract: In order to achieve the strength−ductility synergy and improve the work-hardening capacity, Ti64 based composites with dispersive nanoscaled TiB whiskers inside grains were fabricated by plasma rotating electrode process coupled with spark plasma sintering. Based on the rapid eutectic reaction, the nanoscaled TiB whiskers exhibited ultra-fine network distribution in composite powders. During the spark plasma sintering process, the network dissolved, and TiB followed the Ostwald ripening mechanism and merged along the (100) plane. The intragranular TiB whiskers could significantly refine the primary β grain and α lath. The ultimate tensile strength of the composite with only 2 vol.% TiB whiskers was enhanced to (1123±17) MPa while the elongation was similar to that of the as-sintered Ti64 alloy with approximately 8%. The strength−ductility synergy effect was mainly attributed to the significant grain refinement and the work-hardening ability improvement contributed by intragranular nanoscaled TiB.

Key words: titanium matrix composites; nanoscaled TiB whisker; spark plasma sintering; thermodynamic calculation; microstructure; mechanical properties

1 Introduction

It is an eternal pursuit for the materials research community to achieve the strength−ductility synergy of titanium alloy. Introducing ceramic reinforcements into metal materials is an effective method to improve the strength of titanium alloy [1,2]. However, with the increase in the content of reinforcements, the plasticity of the composites decreases significantly [3]. This is mainly related to the local stress/strain concentration caused by the deformation disharmony between the reinforcements and the matrix [4], which makes composites show the bottleneck problem of strength−plasticity inversion.

Numerous studies have shown that nanometer size reinforcements can strengthen the material effectively [5,6]. In the meantime, the nanoscale reinforcements do not cause severe stress concentration, which is conducive to maintaining the plasticity of the matrix. The results of MU et al [7] showed that only 0.23 vol.% nano-graphite flake can increase the room temperature tensile strength of titanium matrix composites (TMCs) by over 200 MPa. However, the nanometer size reinforcements have a large specific surface area and a strong tendency to agglomerate [8,9]. The agglomeration of reinforcements causes the specific surface area to decrease, thus reducing the strengthening effect [10,11]. Moreover, dislocations can no longer cut or bypass the agglomerated

Corresponding author: Shuai WANG, Tel: +86-451-86413921, E-mail: wangshuai1993@hit.edu.cn;
Lu-jun HUANG, Tel: +86-451-86418836, E-mail: huanglujun@hit.edu.cn
https://doi.org/10.1016/S1003-6326(25)66910-X

reinforcements, which leads to severe stress concentration and deterioration of the ductility.

TiB whisker is one of the most suitable reinforcement candidates for Ti matrix composites [12], so the nanoscaled TiB whiskers are introduced to improve the mechanical properties of Ti-based composites. Recently, using nano-reinforcements as raw materials [3] and using gas atomization [13] to fabricate composite powders have been two main methods of introducing TiB nanometer-size whisker (TiB_{nw}) into the Ti-based composites. However, due to the poor thermal stability of TiB_{nw}, there exists a strong tendency to merge and ripen between TiB_{nw} during the sintering process [14]. As a result, TiB_{nw} tends to aggregate and grow, and the length of TiB_{nw} reaches dozens of microns, reducing the plastic deformation ability of the composites. WANG et al [15] utilized nano-TiB_2 powders and Ti64 alloy powders through ball milling and spark plasma sintering (SPS) to fabricate TiB_{nw} reinforced composites, but TiB_{nw} had a low dispersion and agglomerated at the network boundary.

Plasma rotating electrode process (PREP) melts the titanium matrix and TiB at the same time, and then TiB whiskers precipitate inside the powders during the cooling process, so it can achieve a good dispersion of TiB. Besides, it has the advantage of low content of satellite balls and hollow powders [16,17]. Driven by the above discussion, a two-step strategy combining PREP and SPS was proposed. This study revealed the microstructure formation mechanisms of the pre-alloyed powders and the as-sintered composites, providing guidance for introducing nanometer size reinforcements and the design of nanocomposites.

2 Experimental

The first step was fabricating Ti64−TiB_{nw} pre-alloyed powders by the PREP. The aim was to introduce and disperse TiB_{nw} inside Ti64 matrix powders. The TiB−Ti64 composite billets with 1 vol.% and 2 vol.% TiB were used as raw materials. During the PREP, TiB whisker was melted and separated into a nanometer particle. The oxygen and boron contents of the composite powders (seen in Table S1 in Supplementary Materials (SM)) were within permissible limits. The contents of TiB_{nw} inside the composite were calculated to be 1 vol.% and 2 vol.%, respectively. The second step of rapid sintering and cooling of SPS was used to retain TiB with a nanometer size, and the sintering parameters were 1100 °C for 5 min under 50 MPa with a heating rate of 100 °C/min. Ti64 alloy was fabricated by the same process, for a comparison. The dimensions of the samples fabricated by SPS were *d*40 mm × 20 mm.

The microstructure characterization was performed using a scanning electron microscope (SEM) with an electron backscattered diffraction (EBSD) detector. The samples were inlaid with the electroconductive resins and were polished and etched by Kroll reagent for 5 s. EBSD examinations of composite powders and Ti64−TiB composite were carried out with step sizes of 0.05 and 0.5 μm, respectively. The samples were prepared by mechanochemical polishing. An electron probe X-ray micro-analyzer (EPMA) was adopted to determine the distribution of elements. Transmission electron microscope (TEM) samples of powders and composites were prepared via a focused ion beam and an ion polishing system, respectively. Then, the samples were characterized through TEM. Mechanical properties were tested by a universal testing machine at a strain rate of $5\times10^{-4}\ s^{-1}$. Flat dog-bone specimens with gauge dimensions of 15 mm × 4 mm × 1.5 mm (length × width × thickness) were used. For each kind of material, at least 3 samples were tested.

3 Results and discussion

3.1 Microstructure of Ti64−1TiB_{nw} composite powders

The surface morphology of the Ti64−1vol.%TiB_{nw} (The vol.% was omitted in the following text) and Ti64−2TiB_{nw} composite powders is shown in Fig. S1 in SM and Fig. 1(a), respectively. The composite powders exhibited high sphericity and contained no satellite or irregular powders. These characteristics were beneficial to the mechanical properties of the composites made by those powders. The cross-section microstructure of the composite powders in Fig. 1(b) shows that TiB_{nw} inside the powders was distributed in approximately network structure with diameters of about 3 μm. Compared with the microstructure of the composite billets with microscale TiB inhomogeneous distribution (seen in Fig. S2 in SM),

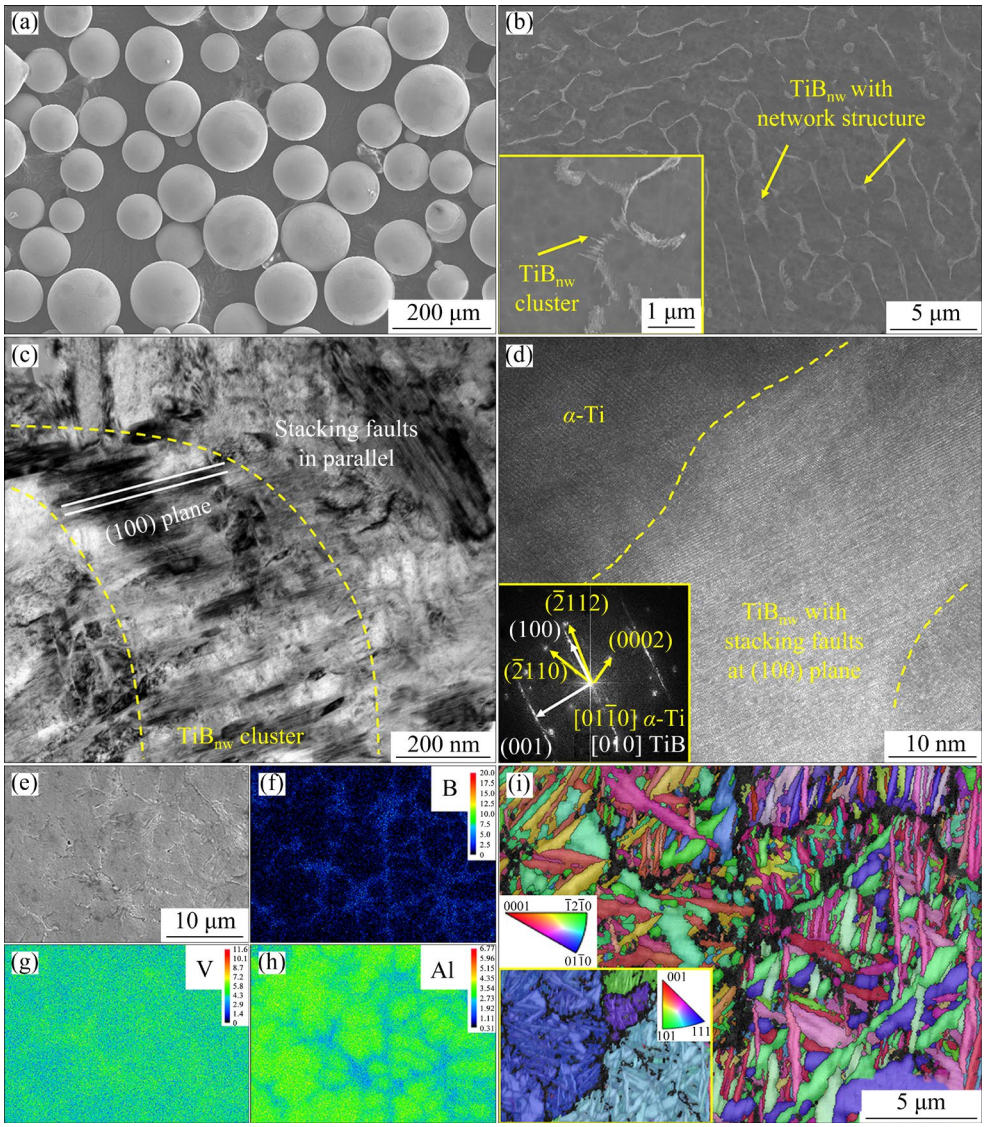

Fig. 1 Microstructure analysis results of Ti64−2TiB_{nw} powders: (a) Surface microstructure; (b) Cross-section microstructure; (c) TEM bright field image of TiB_{nw} and its EDS mapping of B; (d) HRTEM image and FFT image of interface between TiB_{nw} and α-Ti; (e−h) EPMA mappings of cross-section of composite powders; (i) Inverse pole figure (IPF) and primary β grain reconstruction

Fig. 1(b) proves that by the PREP the nano-crystalization of TiB and refinement of the network structure are achieved. The remelted TiB_{nw} was arranged in parallel and formed clusters about 400 nm in size. The arrangement directions of TiB_{nw} among different clusters were random. The TEM image in Fig. 1(c) demonstrates that the length of TiB_{nw} in the cluster was about 300 nm and there were a lot of stacking faults in TiB_{nw}. The FFT spots of TiB_{nw} in Fig. 1(d) stretched along the (100) plane, which means that the stacking faults were determined along the (100) plane. These results prove that TiB_{nw} in the cluster had the same orientation relationship and was arranged along the (100) plane. Figures 1(e−h) exhibit the EPMA mappings of the composite powders, where Al was concentrated in α-Ti inside the network structure. V was segregated at the network boundary, which was the same as the TiB_{nw} distribution. The IPF image in Fig. 1(i) shows that there was no preferred orientation of grain in the composite powders. The primary β grain reconstruction of the composite powders demonstrates that the primary β grains were equiaxed, and TiB_{nw} which was too tiny to be calibrated appeared as a black network structure distributed around the primary β grains. Besides, because of the high cooling rate of the PREP, the α-Ti lamellas were refined with an average

thickness of about 0.2 μm compared with about 10 μm in the composite billets (seen in Fig. S2 in SM). The misorientation angle diagram (seen in Fig. S3 in SM) illustrates that the α lath conformed to the Burgers orientation relationship, which proves that α-Ti was transformed from β-Ti during the cooling process.

3.2 Microstructure of Ti64−TiB_{nw} composites

Figure 2(a) and Fig. S4 in SM exhibit the microstructure of the as-sintered Ti64−TiB_{nw} composites. By comparing Fig. 1(c) and Fig. 2(a), it can be found that after SPS sintering, the TiB_{nw} was distributed homogeneously instead of the network structure, and the α lath thickness was only about 2 μm. In the magnified image in Fig. 2(b), it can be found that TiB_{nw} remained at nanometer size and did not reunite. Some of TiB_{nw} was located inside the grain. TEM image demonstrates that the TiB_{nw} was short needle-like. From Fig. 2(c) it can be found that there was no preferred orientation of grain in the Ti64−2TiB_{nw} composite. The prior β grain was reconstructed by erasing the grain boundaries of the α grains that satisfy the Burgers orientation relationship, and the reconstructed prior β grain is illustrated in Fig. 2(d). It can be found that TiB_{nw} was inside the primary β grain and the size of the primary β grain in the composite was much larger than that in composite powders (Fig. 1(i)). It is proved that during the sintering process, the primary β grains grew and wrapped TiB_{nw} around them. During the cooling process, the α grain transformed from the primary β grain, so some TiB_{nw} existed inside the α grain. The elements in the as-sintered composites were redistributed during the SPS process (seen in Fig. S5 in SM), which proves that elements were diffused during the sintering process.

Figure 3(a) shows that the interface between TiB_{nw} and Ti matrix was clear and straight. The orientation relationship between TiB_{nw} and α-Ti was $(\bar{2}112)_{\alpha\text{-Ti}}//(110)_{TiB_{nw}}$ and $[01\bar{1}0]_{\alpha\text{-Ti}}//[001]_{TiB_{nw}}$. Besides, there were plenty of stacking faults along the (100) plane inside TiB_{nw}. Because of the fast sintering (100 °C/min) and cooling rates (300 °C/min) [18], the B atoms in the (100) plane were prone to loss and misposition during the ripening. It could be seen in Fig. 3(b) that parallel

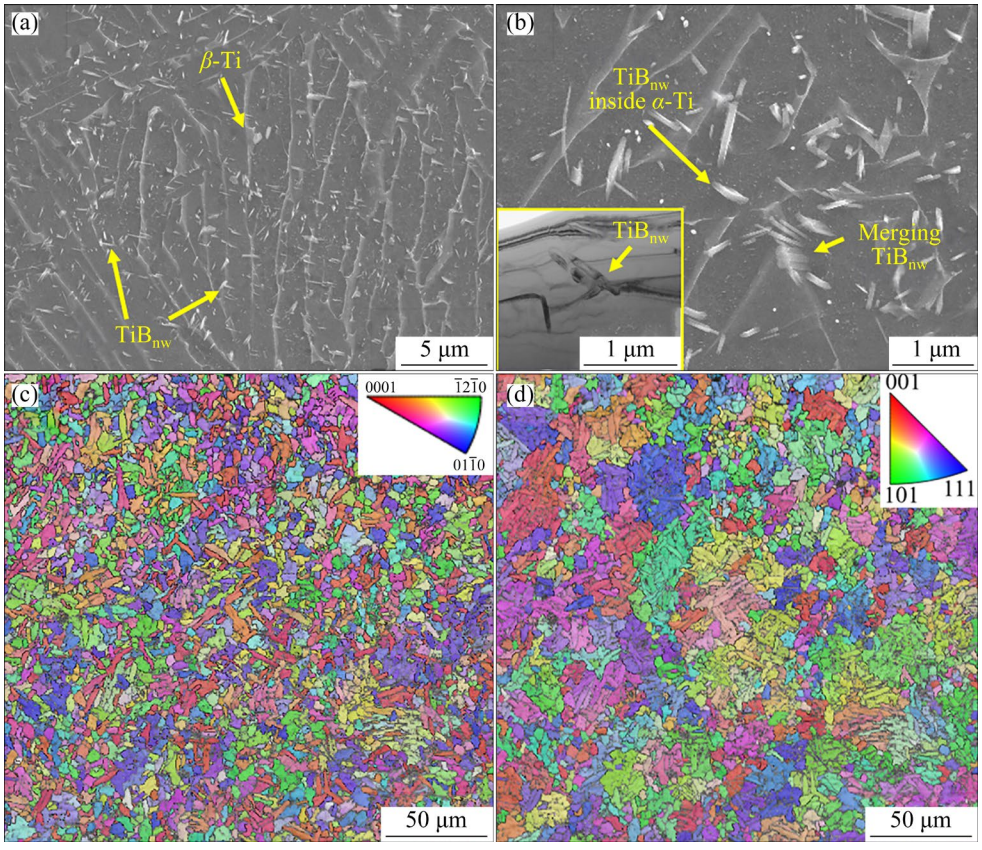

Fig. 2 Microstructure analysis results of Ti64−2TiB_{nw} composite: (a) SEM image; (b) Microstructure of TiB_{nw}; (c) Inverse pole figure (IPF); (d) Primary β grain reconstruction

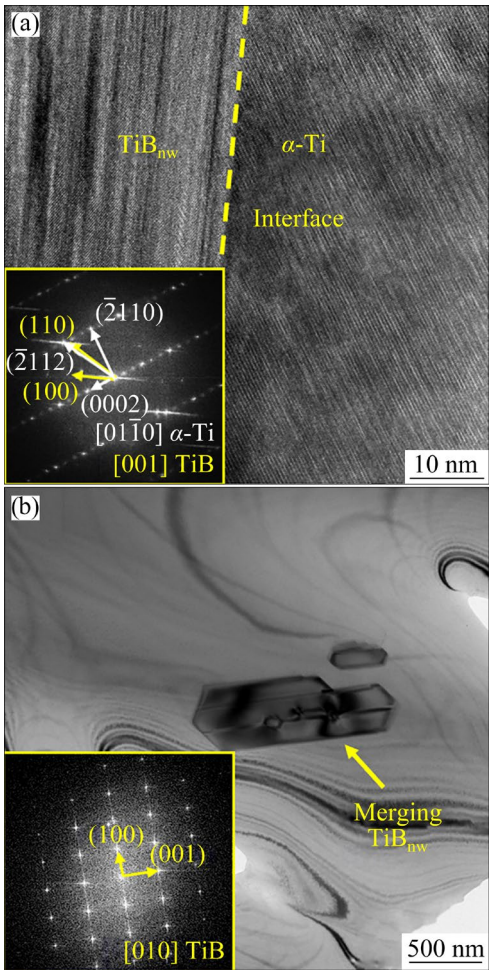

Fig. 3 TEM images of Ti64−2TiB$_{nw}$ composites: (a) HRTEM image and FFT image of interface between TiB$_{nw}$ and α-Ti; (b) Bright-field TEM image and FFT image of merged TiB$_{nw}$

TiB$_{nw}$ merged along the (100) plane during the sintering process. This is because the merging of TiB$_{nw}$ was not a process of nucleation and growth. It was mainly related to the orientation of TiB in composite powders.

3.3 Microstructure evolution mechanism of Ti64−TiB$_{nw}$ composites

The solidification process of powder fabrication was further calculated using the JMatPro software. Owing to the nonequilibrium solidification (The cooling rate of the droplets exceeds 10^5 K/s) [19], the Scheil−Gulliver model [20] was used to calculate the components at the interface between the liquid and β-Ti (Eq. (1)), where k is the mass ratio of the solid and liquid components at the interface; f_s is the solid volume fraction; C_s and C represent the solid content at the interface and initial content of liquid, respectively. The solid volume fraction f_s can be calculated by Eq. (2), where T_f and T_L represent the temperatures of solidus and liquidus at corresponding contents, respectively.

$$C_s = kC(1-f_s)^{k-1} \tag{1}$$

$$f_s = 1-\left(\frac{T_f - T}{T_f - T_L}\right)^{\frac{1}{k-1}} \tag{2}$$

The calculation result of the solidification of Ti64−2TiB$_{nw}$ powders is shown in Fig. 4. During the solidification process, Fig. 4(a) shows that V was

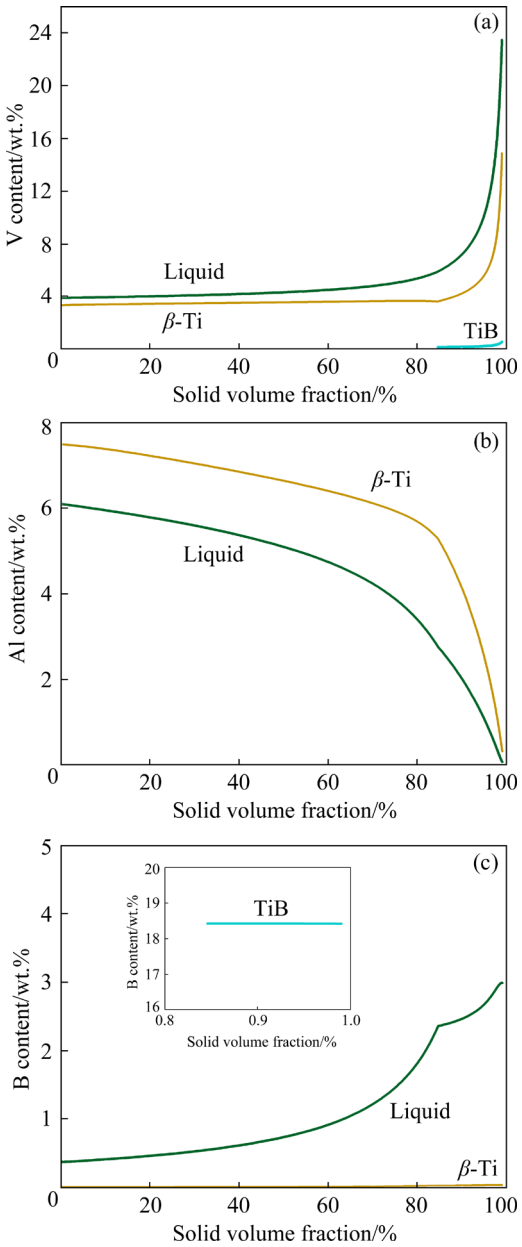

Fig. 4 Element content of each phase with different solid volume fractions: (a) V; (b) Al; (c) B

segregated in the liquid, hence there was more V around β-Ti which precipitated earlier. On the contrary, in Fig. 4(b), Al was concentrated in the β-Ti. Figure 4(c) shows that since the solubility of B in β-Ti was very low, with the solidification process, the content of B in the liquid gradually increased. When the content of B reached about 2.5 wt.%, TiB began to precipitate in the liquid. β-Ti with less B was also precipitated by eutectic reaction with TiB, so the content of B in the liquid still increased. Meanwhile, the B content in the TiB was not affected by the increase of B content in the liquid, and the molar ratio of Ti to B remained 1:1.

Based on the above microstructure analysis and non-equilibrium thermodynamic calculation, Figs. 5(a1−a4) intuitively exhibit the microstructure formation mechanism schematic diagram of composite powder. Before the solidification, Ti droplets spheroidized under the action of surface tension, as shown in Fig. 5(a1). With a large degree of supercooling, β-Ti nucleated plentifully and randomly in the liquid as illustrated in Fig. 5(a2). In Fig. 5(a3), because of different compositions of β-Ti and liquid, V and B atoms were enriched at the interface, and Al atoms were deficient. This resulted in a different concentration of solute in the liquid, leading to the diffusion of atoms in the liquid. Then, as β-Ti grew, the liquid was distributed in a network structure around the proeutectic β-Ti. When the proportion of proeutectic β-Ti was about 85 vol.%, TiB/β-Ti was formed by a eutectic reaction in the liquid and constituted a network structure, as shown in Fig. 5(a4). In account of the large surface energy of TiB_{nw}, eutectic TiB_{nw} in the same grain tended to be arranged in parallel along the (100) plane which had the highest surface energy [14] to reduce the surface energy (seen in Fig. 1(c)). Since the TiB/β-Ti eutectic microstructure nucleated randomly in the liquid, there was no orientation relationship between TiB_{nw} in different clusters. Besides, large supercooling inhibited the growth of TiB_{nw} and maintained it at the nanoscale. The content of V in eutectic structure formed by residual liquid was high and the content of Al was low, which was consistent with the EPMA results in Figs. 1(e−h). Finally, as the temperature was further reduced, β-Ti in the composite powder was transformed into lamellar α-Ti. Because the nanoscaled reinforcements had high surface energy, in order to reduce the total surface energy, the growth of TiB_{nw} mainly followed two mechanisms during the SPS process. The whisker with similar orientation relationship merged along the (100) plane which met in the clusters of the composite powders (seen in Fig. 5(b)). Besides, because of the difference in free energy between the larger TiB_{nw} and smaller TiB_{nw}, Ostwald ripening occurred during the SPS process. The smaller TiB_{nw} dissolved, and then the B atoms spread onto the larger TiB_{nw} and precipitated again. Hence, the network structure became discontinuous. Because the size of the network structure in the composite powders was small, the grown TiB_{nw} located at the boundary of the network finally showed a uniform distribution.

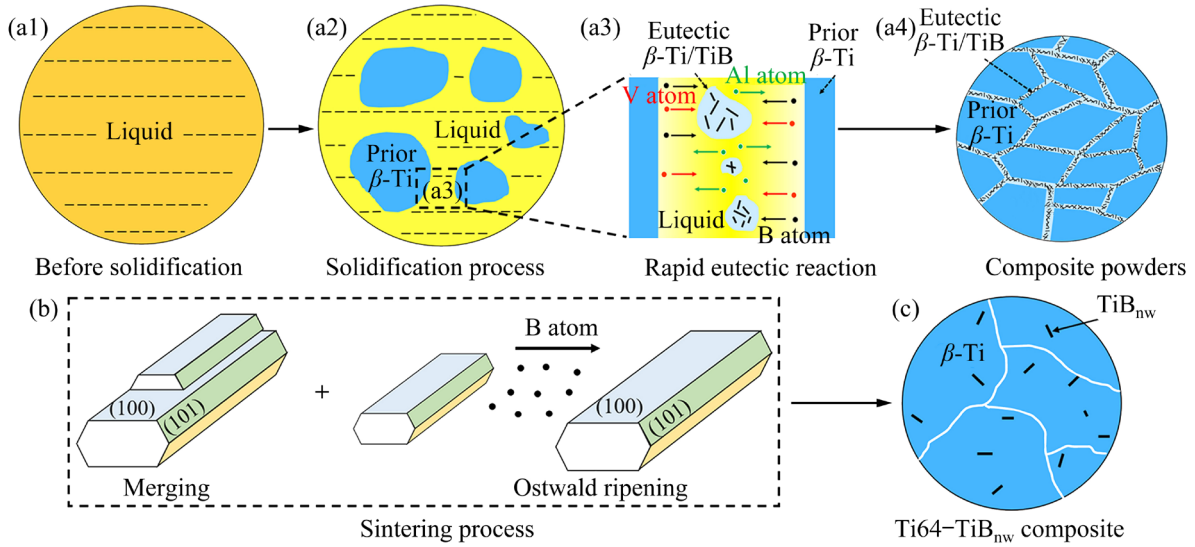

Fig. 5 Illustration of microstructure formation mechanism: (a) Formation of Ti64−TiB_{nw} composite powders during PREP; (b) Evolution mechanism of nano-TiB during SPS; (c) Microstructure of as-sintered composites

3.4 Mechanical properties and strengthening mechanisms of Ti64−TiB_{nw} composites

The tensile engineering stress−strain curves of different samples are plotted in Fig. 6(a). The Ti64−1TiB_{nw} demonstrated a good elongation of (12.5±0.7)% and the strength also exceeded 1000 MPa. The ultimate tensile strength of the Ti64−2TiB_{nw} reached (1123±17) MPa (seen in Table 1), which had an increase of 24.1% with similar elongation compared with the Ti64 alloy. Through the figure of the work-hardening rates, it is found that Ti64−1TiB_{nw} necked until the true strain reached 9%, which was improved by 2 times compared with the Ti64 alloy. The uniform deformation elongation of Ti64−2TiB_{nw} was at least 7%. TiB_{nw} inside the grains acted as a strong obstacle to the dislocation motion and avoided severe dislocation stacking at the grain boundary under low deformation, which could decrease the stress concentration as well as improve the uniform deformation ability of composites. The tensile properties of Ti64 based composites with different kinds of reinforcements are summarized in Fig. 6(b). It shows that the composites in the present study achieved significant improvement in plasticity and maintained the high strengthening efficiency of nanoscale reinforcements.

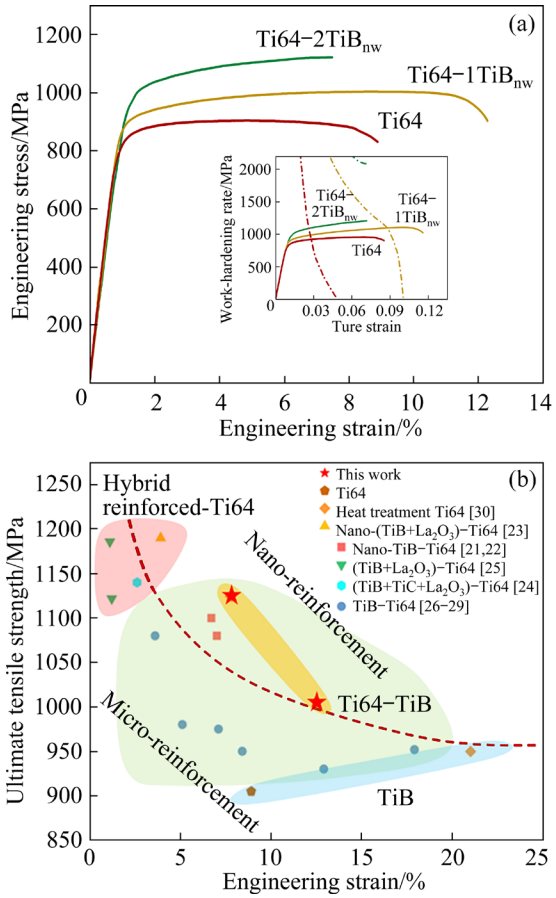

Fig. 6 Engineering stress−strain curves and work-hardening curves of different samples (a), and tensile properties of Ti64 based composites (b) [21−30]

Table 1 Tensile properties of Ti64−TiB_{nw} composites

Sample	Yield strength/MPa	Ultimate strength/MPa	Elongation/%
Ti64	817±5	905±9	8.9±0.4
Ti64−1TiB_{nw}	878±5	1005±10	12.4±0.7
Ti64−2TiB_{nw}	945±7	1123±17	7.7±0.2

The strength of Ti64−TiB_{nw} composites exhibits a significant increase compared with that of Ti64 alloy, and the strengthening effect can be mainly attributed to solution strengthening of oxygen atoms, load transfer effect ($\Delta\sigma_{L-T}$) and grain refinement (Hall−Petch strengthening, $\Delta\sigma_{H-P}$).

The yield strength of Ti64 alloy was 817 MPa. Because of the PREP and low-energy ball milling process, the oxygen content in the composite powders increased from 0.039 wt.% to 0.080 wt.% (shown in Table S1 in SM). Due to the low oxygen content, the strengthening effect of the Ti64 matrix in the composite brought by the solution of oxygen atoms could be expressed as [3]

$$\sigma_m=\sigma_y+0.02G(c_m^k-c^k) \quad (3)$$

where σ_m is the yield strength of Ti64 matrix in the composite, σ_y is the yield strength of the Ti64 alloy, G is the shear modulus, c_m is the oxygen content in the composite, c is the oxygen content in the Ti64 alloy, and k is the concentration exponent [3]. Because the oxygen atoms occupy interstitial positions, k should be 0.5. As a result, the yield strength of the Ti64 matrix in the composite increased to 830 MPa.

The TiB_{nw} with uniform distribution had a high aspect ratio (about 15 on average), which could transfer the load effectively. The shear lag model is suitable for the composite with uniformly distributed reinforcement, so we employed Eq. (4) [31] to quantitatively estimate the strengthening effect of load transfer:

$$\Delta\sigma_{L-T}=0.5\sigma_m VSw \quad (4)$$

where V is the volume fraction of TiB_{nw}, S is the average aspect ratio of TiB_{nw}, and w is the orientation factor of TiB_{nw}. TiB_{nw} in the composites

was distributed randomly. According to WANG et al [32], the value of w should be 0.27. The yield strength contributed by the load transfer effect was calculated as about 34 MPa.

Figure 2(c) and Fig. S6 in SM show that TiB_{nw} can significantly refine the α lath and prior β grain. This is because the uniform TiB_{nw} can provide an energetically preferred nucleation site for the α lath. When sintering, TiB_{nw} can inhibit the grain boundary migration, which can hinder the overgrowth of the prior β grain. The Hall−Petch strengthening effect can be expressed by

$$\Delta\sigma_{H-P}=K(\lambda_1^{-0.5}-\lambda_2^{-0.5}) \quad (5)$$

where K is the associated Hall−Petch constant of Ti64 alloy (510.1 MPa·μm$^{0.5}$ [28]), and λ_1 and λ_2 are α lath thicknesses of the Ti64 alloy and composite, respectively. Their α lath thicknesses were 13.28 and 4.58 μm, respectively. The grain refinement effect contributed to the yield strength of about 98 MPa. As a result, the yield strength of the Ti64−2TiB_{nw} composite is calculated as 962 MPa, which is in good agreement with the measured results (945 MPa).

There were a lot of tearing edges and fine dimples in the fracture of Ti64−2TiB_{nw} in Fig. 7(a),

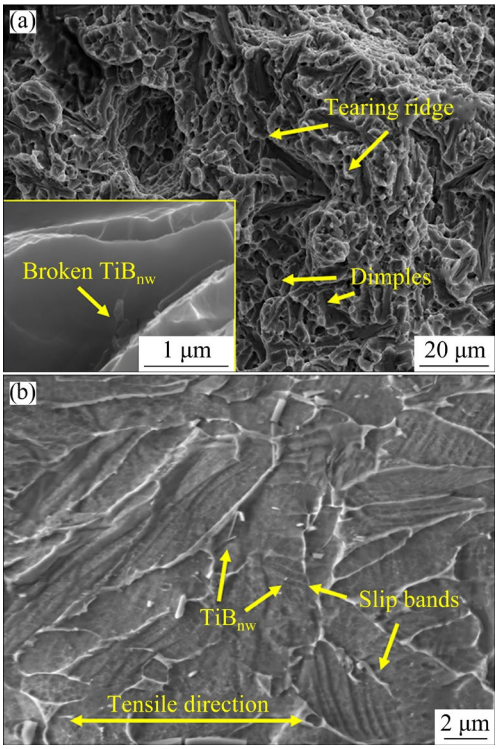

Fig. 7 Fracture morphology of Ti64−2TiB_{nw}: (a) Fractography; (b) Microstructure of sample near fractured surface

which proved that the composite had good tensile ductility. Besides, the grain refinement caused by TiB_{nw} was also conducive to the uniform deformation ability, which can significantly improve the uniform plasticity and ductility of the composite. The fractured TiB_{nw} in Fig. 7(a) indicates that TiB_{nw} was well combined with the matrix interface and could bear the load. Besides, the slip bands could pass through TiB_{nw} which was located in grain in Fig. 7(b), reducing the source of microcracks in the composites. The movement of the slip bands could still be hindered under high strain by the complete TiB_{nw}. It could relieve the stress concentration at grain boundaries and enhance the plasticity and work-hardening ability of the composites.

4 Conclusions

(1) TiB_{nw} with ultra-fine network structure (about 3 μm) was planted into the Ti64 composite powder based on the hypoeutectic reaction. To reduce the surface energy, the eutectic TiB_{nw} was arranged along the (100) plane and formed nanoclusters.

(2) During the SPS process, the network dissolved, and TiB_{nw} followed the Ostwald ripening mechanism and merged, realizing intragranular dispersive distribution.

(3) The ultimate tensile strength of the Ti64−2TiB_{nw} composites increased from 905 to 1123 MPa while the plasticity was nearly the same as that of the Ti64 alloy. The intragranular TiB_{nw} significantly enhanced the work hardening rate of the composites and refined the α lath from 13.28 to 4.58 μm.

CRediT authorship contribution statement

Wen-qi LIU: Investigation, Data curation, Writing – Original draft; **Shuai WANG:** Writing – Review & editing, Supervision; **Xin CHEN:** Methodology; **Lu-jun HUANG:** Conceptualization; **Jia-yi JIN:** Investigation; **Feng-bo SUN:** Validation, Formal analysis; **Wei-hang LU:** Investigation; **Lin GENG:** Project administration.

Declaration of competing interest

The authors declare that they have no known competing financial interests or personal relationships that could have appeared to influence the work reported in this paper.

Acknowledgments

This work was supported by the National Key R&D Program of China (No. 2022YFB3707402), the National Natural Science Foundation of China (Nos. 52301189, U22A20113), and the Natural Science Foundation of Heilongjiang Province, China (No. LH2023E031).

Supplementary Materials

Supplementary Materials in this paper can be found at: http://tnmsc.csu.edu.cn/download/13-p3751-2024-0063-Supplementary_Materials.pdf.

References

[1] ZHENG Shi-qi, REMENTERIA R, KAN Wen-bin, XU Ming-jie, HUANG Jin, HUANG Yu, PAN Xiao-qing, APELIAN D, LIANG Yong-feng, LIN Jun-pin, PEREZ M, LI Xiao-chun. Nanoparticle enabled high performance high modulus steels [J]. Scripta Materialia, 2021, 201: 113954.

[2] HUANG Lu-jun, AN Qi, GENG Lin, WANG Shuai, JIANG Shan, CUI Xi-ping, ZHANG Rui, SUN Feng-bo, JIAO Yang, CHEN Xin, WANG Cun-yu. Multiscale architecture and superior high-temperature performance of discontinuously reinforced titanium matrix composites [J]. Advanced Materials, 2021, 33(6): e2000688.

[3] HUANG Li-qing, WANG Li-hua, QIAN Ma, ZOU Jin. High tensile-strength and ductile titanium matrix composites strengthened by TiB nanowires [J]. Scripta Materialia, 2017, 141: 133−137.

[4] XU Rong-jun, LIU Bin, LIU Yong, CAO Yuan-kui, GUO Wen-min, NIE Yan, LIU Shi-feng. High temperature deformation behavior of in-situ synthesized titanium-based composite reinforced with ultra-fine TiB whiskers [J]. Materials, 2018, 11(10): E1863.

[5] XIE Ke-wei, NIE Jin-feng, HU Kai-qi, MA Xia, LIU Xiang-fa. Improvement of high-temperature strength of 6061 Al matrix composite reinforced by dual-phased nano-AlN and submicron-Al_2O_3 particles [J]. Transactions of Nonferrous Metals Society of China, 2022, 32(10): 3197−3211.

[6] KÜRNSTEINER P, WILMS M B, WEISHEIT A, GAULT B, JAGLE E A, RAABE D. High-strength Damascus steel by additive manufacturing[J]. Nature, 2020, 582: 515−519.

[7] MU X N, ZHANG H M, CHEN P W, CHENG X W, LIU L, GE Y X, XIONG N, ZHENG Y C. Achieving high performance in graphite nano-flakes reinforced titanium matrix composites through a novel reaction interface design [J]. Carbon, 2021, 175: 334−351.

[8] LI Jian-yu, LÜ Shu-lin, CHEN Lu, LIAO Qiao, GUO Wei, WU Shu-sen. Influence of squeeze casting pressure on nanoparticle distribution and mechanical properties of nano-SiC_p/AlCu composites assisted with ultrasonic vibration [J]. Transactions of Nonferrous Metals Society of China, 2023, 33(7): 1977−1987.

[9] LIU Wei-qing, CAO Che-zheng, XU Jia-quan, WANG Xiao-jun, LI Xiao-chun. Molten salt assisted solidification nanoprocessing of Al−TiC nanocomposites [J]. Materials Letters, 2016, 185: 392−395.

[10] KAIRA C S, de ANDRADE V, SINGH S S, KANTZOS C, KIRUBANANDHAM A, de CARLO F, CHAWLA N. Probing novel microstructural evolution mechanisms in aluminum alloys using 4D nanoscale characterization [J]. Advanced Materials, 2017, 29(41): 1703482.

[11] LEE W M, ZIKRY M A. Modeling the interfacial plastic strain incompatibilities associated with dispersed particles in high strength aluminum alloys [J]. Acta Materialia, 2012, 60(4): 1669−1679.

[12] LIAN Qi-hao, ZHANG Chang-jiang, FENG Hong, YANG Zhen-bo, ZHANG Shu-zhi, HAN Jian-chao, WANG Tao, PENG Fan, CAO Peng. Hot deformation temperature and pre-deformation effect on silicide precipitation behavior of (TiB+Y_2O_3)/near α-Ti matrix composite [J]. Transactions of Nonferrous Metals Society of China, 2023, 33(9): 2660−2671.

[13] PAN Deng, LI Shu-feng, LIU Lei, ZHANG Xin, LI Bo, CHEN Biao, CHU Ming-qiang, HOU Xiao-dong, SUN Zhong-gang, UMEDA J, KONDOH K. Enhanced strength and ductility of nano-TiB_w-reinforced titanium matrix composites fabricated by electron beam powder bed fusion using Ti6Al4V−TiB_w composite powder [J]. Additive Manufacturing, 2022, 50: 102519.

[14] LI Shao-peng, HAN Yuan-fei, WANG Xiao-yan, HUANG Guang-fa, FANG Min-han, SHI Hui-gang, LE Jian-wen, LU Wei-jie. Novel strategy of planting nano-TiB fibers with ultra-fine network distribution into Ti-composite powder and its thermal transition mechanism [J]. Composites Communications, 2022, 29: 101002.

[15] WANG Qiang, ZHANG Zhao-hui, SU Tie-jian, CHENG Xing-wang, LI Xian-yu, ZHANG Shun-zhong, HE Jian-ye. A TiB whisker-reinforced titanium matrix composite with controllable orientation: A novel method and superior strengthening effect [J]. Materials Science and Engineering: A, 2022, 830: 142309.

[16] CHEN G, ZHAO S Y, TAN P, WANG J, XIANG C S, TANG H P. A comparative study of Ti−6Al−4V powders for additive manufacturing by gas atomization, plasma rotating electrode process and plasma atomization [J]. Powder Technology, 2018, 333: 38−46.

[17] LIU Yang, ZHAO Xiao-hao, LAI Yun-jin, WANG Qing-xiang, LEI Li-ming, LIANG Shu-jin. A brief introduction to the selective laser melting of Ti6Al4V powders by supreme-speed plasma rotating electrode process [J]. Progress in Natural Science: Materials International, 2020, 30(1): 94−99..

[18] ZHANG Fa-ming, REICH M, KESSLER O, BURKEL E. The potential of rapid cooling spark plasma sintering for metallic materials [J]. Materials Today, 2013, 16(5): 192−197.

[19] WOSCH E. Rapid solidification of steel droplets in plasma rotating electrode process [J]. Metal Powder Report, 1997, 51(1): 35.

[20] LIN X, YUE T M, YANG H O, HUANG W D. Phase evolution in laser rapid forming of compositionally graded Ti−Ni alloys [J]. Journal of Engineering Materials and

Technology, 2009, 131(4): 041002.
[21] WANG F D, MEI J F, WU X H. Direct laser fabrication of Ti6Al4V/TiB [J]. Journal of Materials Processing Technology, 2008, 195(1/2/3): 321−326.
[22] XUE Ai-tang, LIN Xin, WANG Li-lin, WANG Jian, HUANG Wei-dong. Influence of trace boron addition on microstructure, tensile properties and their anisotropy of Ti6Al4V fabricated by laser directed energy deposition [J]. Materials & Design, 2019, 181: 107943.
[23] LI Shao-peng, WANG Xiao-yan, WEI Zi-chao, HAN Yuan-fei, SHI Hui-gang, LE Jian-wen, HUANG Guang-fa, ZHANG Di, LU Wei-jie. Simultaneously improving the strength and ductility of the as-sintered (TiB+La_2O_3)/Ti composites by in-situ planting ultra-fine networks into the composite powder [J]. Scripta Materialia, 2022, 218: 114835.
[24] QIU Pei-kun, LI Hong, SUN Xiang-long, HAN Yuan-fei, HUANG Guang-fa, LU Wei-jie, ZHANG Di. Reinforcements stimulated dynamic recrystallization behavior and tensile properties of extruded (TiB+TiC+La_2O_3)/Ti6Al4V composites [J]. Journal of Alloys and Compounds, 2017, 699: 874−881.
[25] LIU Yu-yu, JIANG Wei, CHEN Zheng, XU Quan, ZHANG Zhi-liang, HE Jian-ying. Optimization of processing parameters and microstructure evolution of (TiB+La_2O_3)/Ti6Al4V manufactured by laser melting deposition [J]. Journal of Materials Research and Technology, 2023, 24: 8086−8097.
[26] REN Ze-qi, LIU Wen-qi, AN Qi, CHEN Xiao-dong, WEI Guo-liang, CHEN Run, ZHANG Rui, HUANG Lu-jun, GENG Lin. Microstructures and tensile properties of low-cost TiB_w/Ti−6Al−4V composites by vacuum reactive hot pressing [J]. Vacuum, 2023, 211: 111921.
[27] LUAN J H, JIAO Z B, HEATHERLY L, GEORGE E P, CHEN G, LIU C T. Effects of boron on the fracture behavior and ductility of cast Ti−6Al−4V alloys [J]. Scripta Materialia, 2015, 100: 90−93.
[28] SEN I, TAMIRISAKANDALA S, MIRACLE D B, RAMAMURTY U. Microstructural effects on the mechanical behavior of B-modified Ti−6Al−4V alloys [J]. Acta Materialia, 2007, 55(15): 4983−4993.
[29] HUANG L J, GENG L, WANG B, XU H Y, KAVEENDRAN B. Effects of extrusion and heat treatment on the microstructure and tensile properties of in situ TiB_w/Ti6Al4V composite with a network architecture [J]. Composites Part A: Applied Science and Manufacturing, 2012, 43(3): 486−491.
[30] WANG Zhao, BIAN Hai-rong, LU Hai-fei, MA Guang-yi, WU Dong-jiang, LUO Kai-yu, LU Jin-zhong. Significant improvement in the strength−toughness and isotropy of laser powder bed fused Ti6Al4V alloy by combining heat treatment with subsequent laser shock peening [J]. Materials Science and Engineering: A, 2023, 880: 145365.
[31] WANG Shuai, HUANG Lu-jun, AN Qi, MA Zi-shuo, ZHANG Rui, PENG Hua-xin, GENG Lin. Strength−ductility synergy of in-situ TiB/Ti6Al4V composites with tailored hierarchical TiB distributions [J]. Ceramics International, 2022, 48(23, Part A): 35069−35075.
[32] WANG Ji-heng, GUO Xiang-long, QIN Ji-ning, ZHANG Di, LU Wei-jie. Microstructure and mechanical properties of investment casted titanium matrix composites with B_4C additions [J]. Materials Science and Engineering: A, 2015, 628: 366−373.

基于等离子旋转电极雾化和放电等离子烧结实现 Ti64 复合材料中纳米 TiB 的弥散分布

刘文齐[1]，王 帅[1]，陈 昕[1]，黄陆军[1,2]，金嘉熠[1]，孙枫泊[1]，鲁伟航[1]，耿 林[1,2]

1. 哈尔滨工业大学 材料学科与工程学院，哈尔滨 150001；
2. 哈尔滨工业大学 材料结构精密焊接与连接全国重点实验室，哈尔滨 150001

摘 要：为了同步提升钛基复合材料的强度、塑性和加工硬化能力，采用等离子旋转电极雾化和放电等离子烧结制备了纳米 TiB 晶须在晶内呈弥散分布的 Ti64 复合材料。由于快速共晶反应，复合粉末中的纳米 TiB 晶须呈超细网状结构分布。在放电等离子烧结过程中，复合粉末中的网状结构消失，TiB 遵循 Ostwald 熟化机制并沿(100)晶面合并。同时，位于晶内的 TiB 晶须可以显著细化原始 β 晶粒以及 α 片层。在仅含 2% TiB (体积分数)晶须的条件下，复合材料的极限抗拉强度提升至(1123±17) MPa，同时伸长率约为 8%，与烧结态 Ti64 合金的接近。这种强度和塑性协同提升效应主要归结于显著的晶粒细化以及晶内纳米 TiB 引起的加工硬化能力的提升。

关键词：钛基复合材料；纳米 TiB 晶须；放电等离子烧结；热力学计算；显微组织；力学性能

(Edited by Wei-ping CHEN)